Fiber-optic probe design and optical property recovery algorithm for optical biopsy of brain tissue

Derek J. Cappon
Thomas J. Farrell
Qiyin Fang
Joseph E. Hayward

Fiber-optic probe design and optical property recovery algorithm for optical biopsy of brain tissue

Derek J. Cappon,[a] Thomas J. Farrell,[a] Qiyin Fang,[b] and Joseph E. Hayward[a,b]
[a]McMaster University, Department of Medical Physics and Applied Radiation Sciences, 1280 Main Street W, Hamilton, Ontario L8S 4K1, Canada
[b]McMaster University, Department of Engineering Physics, 1280 Main St W, Hamilton, Ontario L8S 4L7, Canada

Abstract. Optical biopsy techniques offer a minimally invasive, real-time alternative to traditional biopsy and pathology during tumor resection surgery. Diffuse reflectance spectroscopy (DRS) is a commonly used technique in optical biopsy. Optical property recovery from spatially resolved DRS data allows quantification of the scattering and absorption properties of tissue. Monte Carlo simulation methods were used to evaluate a unique fiber-optic probe design for a DRS instrument to be used specifically for optical biopsy of the brain. The probe diameter was kept to a minimum to allow usage in small surgical cavities at least 1 cm in diameter. Simulations showed that the close proximity of fibers to the edge of the probe resulted in boundary effects due to reflection of photons from the surrounding air–tissue interface. A new algorithm for rapid optical property recovery was developed that accounts for this reflection and therefore overcomes these effects. The parameters of the algorithm were adjusted for use over the wide range of optical properties encountered in brain tissue, and its precision was evaluated by subjecting it to random noise. This algorithm can be adapted to work with any probe geometry to allow optical property recovery in small surgical cavities. © 2013 Society of Photo-Optical Instrumentation Engineers (SPIE) [DOI: 10.1117/1.JBO.18.10.107004]

1 Introduction

Intraoperative guidance of tumor resection surgery is an emerging technology that is being adopted in many different forms in operating rooms around the world.[1–3] This has widespread applications, but can be especially important during the resection of glioblastomas: grade IV brain tumors with a poor prognosis. These infiltrating glial tumors originate from normal brain cells and have an appearance that is similar to the surrounding tissue,[4] especially in the margins, meaning that optimal resection is difficult to achieve. Studies have indicated that complete resection is beneficial to patients presenting with both low- and high-grade gliomas.[5,6]

Optical spectroscopy is a promising technique that has been investigated for intraoperative use. It allows rapid, minimally invasive analysis of the composition of tissue—a process commonly referred to as optical biopsy. Various optical biopsy modalities have been developed and investigated in different diseases, including cancers of the breast,[7,8] oral mucosa,[9,10] and brain.[11] Fiber-optic probes are typically used to both deliver light to the target tissue and collect the resulting optical signal for analysis. These spectroscopy devices offer a low-cost alternative to more expensive imaging techniques such as intraoperative magnetic resonance imaging[3,4] and can be designed so that they do not require the injection of exogenous fluorophores as is often the case in intraoperative fluorescence imaging.[12,13]

Because the area of tissue investigated by these devices is limited, they are not suited for wide-field applications but are ideal for localized investigations within small, well-defined areas such as surgical cavities.

Diffuse reflectance spectroscopy (DRS) is a technique that is often used during optical biopsy.[14–16] The reflectance spectra obtained with this modality can be used to extract quantitative information on the scattering and absorption of light in tissue—a process known as optical property recovery. The optical properties recovered by this process are the absorption coefficient μ_a and reduced scattering coefficient $\mu_s' = \mu_s(1 - g)$, where μ_s is the scattering coefficient and g is the anisotropy coefficient of the tissue.

Many different methods have been developed for the determination of tissue optical properties. Some rely on time-resolved (time or frequency domain) measurements, while others are based on steady-state measurement of DRS signals. Time-resolved techniques use time-dependent diffusion theory or Monte Carlo modeling to predict the time of flight of photons, and fit these data to experimental results. Time-domain methods use a very short (picosecond) light pulse and measure how long it takes photons to reach the detector, while frequency-domain methods use a modulated light source and match the measured phase shift, amplitude modulation, and/or steady-state intensity of the reflectance with those predicted by the Fourier transform of the time-domain diffusion theory formula. An example of a time-domain system for optical property recovery in human tissue is described by Svensson et al.,[17] while examples of

Address all correspondence to: McMaster University, Department of Medical Physics and Applied Radiation Sciences, 1280 Main St W, Hamilton, Ontario, Canada. Tel: +905-525-9140 x26159; Fax: 905-522-5982; E-mail: cappond@mcmaster.ca

frequency-domain systems are given by Fishkin et al.[18] and Gurfinkel et al.[19]

Some of the methods used to measure steady-state tissue reflectance include total reflectance measurements with integration spheres, spectrally constrained diffuse reflectance measurements, and spatially resolved diffuse reflectance measurements. When performing spectrally constrained diffuse reflectance measurement, the reflectance spectrum is measured using a single detector fiber located some distance from a source (illumination) fiber. A diffusion theory model of the reflectance calculated using *a priori* knowledge of the scattering spectra of the chromophores assumed to be present in the tissue is then fitted to this measured spectrum.[20] Recently, this method was expanded to more than one radial distance to allow use over a wider range of optical properties.[21]

Spatially resolved steady-state DRS (SR-DRS), on the other hand, uses multiple detector fibers placed at different distances from a source to obtain measurements of the reflectance versus radial distance. Spatial reflectance curves predicted using diffusion theory or Monte Carlo modeling are then fitted to these data. When using a broadband light source and spectrometer, fitting must be performed at each different wavelength of interest to determine the absorption and scattering spectra.

In this study, optical properties are recovered from SR-DRS data. When compared to time-resolved techniques, this method uses simpler, generally less expensive equipment, requiring only a fiber-optic probe and spectrometer (either an imaging spectrometer or a separate single-channel spectrometer for each source–detector separation). This method differs from the spectrally constrained technique in that it can be used to extract optical properties without advance knowledge or assumptions of which chromophores are present in the tissue.

Monte Carlo simulation is an effective tool to study photon transport in tissue.[22,23] It offers advantages over diffusion theory and other numerical methods that are accurate only for large source–detector separations and correspondingly large probes. Probability distributions are used to describe local interactions of photons with their surroundings, and the individual histories of many different photons are simulated as they travel through tissue. Optical properties can be effectively recovered from SR-DRS data using Monte Carlo simulations.[24,25]

Our group is working to develop an optical biopsy instrument that makes use of SR-DRS measurements to recover the optical properties of brain tissue. This instrument will later be combined with a time-resolved fluorescence spectroscopy (TRFS) system that is being developed concurrently.[26] Because both DRS and TRFS make use of fiber-optic probes, integrating two such systems is a relatively straightforward task. Potential benefits of this integration include two independent sources of contrast for tissue composition analysis and the possibility of intrinsic fluorescence spectroscopy (IFS). IFS is a technique explored by many other groups in this field,[7,27–31] which uses DRS data to correct distortions in fluorescence spectra that result from scattering and absorption of light in tissue.

The purpose of this paper is to present the development of a unique small-diameter fiber-optic probe design meant for DRS of brain tissue in small surgical cavities and to present a modified optical property recovery algorithm developed for use with this probe design. This expands upon previous results[32] by demonstrating (through simulations) the incompatibility of previous optical property recovery algorithms with the new probe design

and documents the optimization of the parameters of the Monte Carlo simulations used in the algorithm.

2 Models and Methods

2.1 Monte Carlo Models

All Monte Carlo codes used in this study simulated a single layer of tissue with homogeneous optical properties and a refractive index of 1.4. The same procedures were used for selecting photon step size, absorption/scattering, and boundary interactions as those described by Wang et al.[23] The Henyey–Greenstein phase function[33] was used to calculate the scattering angle of photons[23,34,35] and all simulations assumed an anisotropy factor (g) of 0.9. This was considered appropriate as the anisotropy factor of brain tissue is close to 0.9 across the spectral range of interest.[36]

The use of a single anisotropy coefficient is a common approach taken when modeling reflectance data.[14,15,27] Although decreasing $|g|$ means that scattering is more isotropic and therefore shifts spatial reflectance curves toward shorter source–detector separations, it has been demonstrated that when $g > 0.8$, changes to the anisotropy factor have a minor effect on the reflectance.[24,25]

The absorption and reduced scattering coefficients (μ_a and μ_s') used in these simulations were chosen to be similar to those of human brain tissue (both gray and white matter) at various wavelengths. The wavelengths investigated in this study were from 360 to 950 nm, as these are the limits of the spectrometer to be used in the final DRS instrument. The optical properties of brain tissue at these wavelengths were taken from results published in a study by Yaroslavsky et al.,[36] and representative values are shown in Table 1. These values were used to define the range over which a DRS instrument used in the brain would be expected to operate, and we therefore ensured that the optical property algorithms were effective within this range.

A number of Monte Carlo–based techniques are described in this section. The first is the Mono Monte Carlo method, a technique for determining optical properties from SR-DRS data using the results of a single Monte Carlo simulation. This technique was used to simulate how removing detector fibers from a DRS fiber-optic probe design would affect the recovery of optical properties. As will be shown in Sec. 3, simulations indicated that the close proximity of detector fibers to the edge of the probe invalidated the assumption of a uniform refractive index at the tissue surface. This is a common assumption when modeling reflectance in tissue[23,37,38] and is necessary

Table 1 Optical properties of brain tissue (Ref. 36).

Tissue	λ (nm)	μ_a (mm^{-1})	μ_s' (mm^{-1})
White matter	360	0.31	2.34
	630	0.02	0.99
	950	0.04	0.61
Gray matter	360	0.23	12.30
	630	0.08	6.54
	950	0.10	3.60

for the spatial invariance required by the Mono Monte Carlo method. This motivated the development of a modified algorithm for the recovery of optical properties from DRS data, one that considers the true geometry of the probe and, most importantly, the different refractive indices encountered by photons leaving the tissue surface (described in Sec. 2.5).

To test the validity of these Monte Carlo methods, results of the basic Monte Carlo code were compared with those from the MCML code published by Wang et al.[23] and the results of diffusion theory calculations. The extended source diffusion theory model described by Farrell et al.[37] was used.

2.2 Optical Property Recovery from the Results of a Single Monte Carlo Simulation

An inverse Monte Carlo algorithm was used to recover optical properties from SR-DRS spectra. This algorithm uses the iterative Marquardt–Levenberg curve-fitting routine to fit Monte Carlo–generated spatial reflectance curves to experimental data (in this work, simulated data were used in place of experimental data). Since running repeated Monte Carlo simulations is prohibitively slow, a Mono Monte Carlo technique was used, based on the condensed simulation approach introduced by Graaff et al.[24] and adapted by others.[25,38]

This approach used a single reference simulation with optical properties μ_{aref} and μ'_{sref} to determine the number of interactions of each photon within the medium. In such a simulation, changing the scattering coefficient only affects the path lengths followed by photons between interactions. For this reason, the results of a single Monte Carlo simulation can be applied for a sample with new optical properties so long as the distances in the original simulation can be scaled and the new albedo $c = \mu_s/(\mu_a + \mu_s)$ is less than or equal to c_{ref}, the albedo of the reference simulation.[24]

The reference simulation was run for 2×10^9 photons with optical properties $\mu_{aref} = 0$ and μ'_{sref}. Note that any value of μ_{aref} could be used, but setting the absorption to 0 guaranteed that c_{ref} was always higher than or equal to c. Upon exiting the tissue, each photon was binned in a grid location defined by ρ_{ref}, the photon's radial distance from the source, and n_{scat}, the number of scattering events it experienced while travelling through the tissue. This provided a table of the reflectance R_{ref} at discrete values of ρ_{ref} and n_{scat} as illustrated in Fig. 1.

This grid could then be used to determine the reflectance for a sample with optical properties μ_a and μ'_s by applying Eq. (1). First, each value of R_{ref} was multiplied by the new albedo raised to the power of n_{scat}. This could be done since the albedo provides a measure of the fraction of photons that are scattered out of a collimated beam in one path length. The grid was then collapsed down to one dimension by taking the sum along each column.

$$R(\rho) = \sum_{n_{scat}} R_{ref}\left[\rho \cdot \left(\frac{\mu_t}{\mu_{tref}}\right), n_{scat}\right] \cdot \left[\frac{\mu_s}{\mu_a + \mu_s}\right]^{n_{scat}}. \quad (1)$$

The reflectance at a given source–detector distance (SDD) $R(\rho)$ could be found after first scaling the distances in the collapsed grid by the ratio of the new mean free path ($1/\mu_t$) to the mean free path used in the reference simulation ($1/\mu_{tref}$). Because scoring was performed radially, the boundaries of each bin were concentric circles around a central (source) point. The scaling procedure moved the boundaries of the
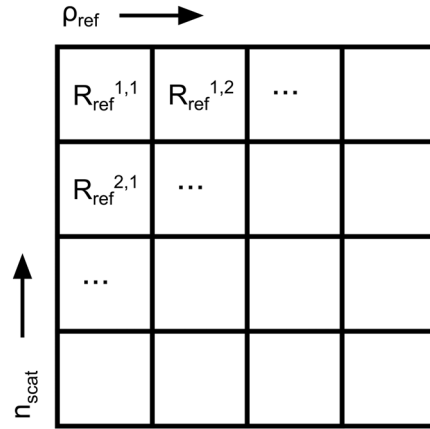

Fig. 1 Photon scoring grid used to set up the Mono Monte Carlo method. ρ_{ref} is the radial distance from the source at which a photon exited the tissue and n_{scat} is the total number of scattering events the photon experienced.

bins inward or outward and therefore changed the bin positions and widths (areas). To compensate for this, each extracted reflectance value was normalized by the total area of the scaled bin in which it was scored. This area was found by subtracting the area of the circle defined by the inner boundary from the area of the circle defined by the outer boundary.

Values of ρ were used that corresponded to the positions of optical fibers in a DRS probe, and extracted spatial reflectance curves were fitted to SR-DRS data using the Marquardt–Levenberg curve-fitting algorithm. When used with experimental reflectance data, this inversion procedure allows determination of the optical properties of a measured sample.

2.3 Reducing the Probe Size

Practically, to allow ease of use in small surgical cavities, the diameter of the fiber-optic probe will be kept quite small. This meant that any data being fitted could contain only a few short SDDs near the front of a radially resolved reflectance curve. A simulation-based procedure was used to observe the precision in the recovered optical properties as the outermost SDD was reduced.

To do so, a low noise reflectance curve was generated (using Monte Carlo methods), and random Gaussian noise was added with standard deviations of 5, 10, and 15% commensurate with experimental conditions observed during preliminary investigations. These data were fitted using the Mono Monte Carlo method to recover μ_a and μ'_s. This was repeated 1000 times, and the standard deviation in the recovered optical properties was determined. Previous investigations suggested that one thousand repetitions were sufficient to ensure that the uncertainties in the results approached their limiting values. This entire process was repeated as the maximum radial distance was reduced, for various input optical properties. In these simulations, reflectance data were generated at evenly spaced distances of 0.3 mm, corresponding to typical fiber diameters.

Reducing the maximum SDD in the probe had the additional effect of changing the depth of tissue probed by reflectance measurements. This was investigated by simulating a probe containing a single source and detector and placing the detector at varying distances from the source. For any photon that was eventually collected by the detector, its depth was recorded

each time it passed below a target radial distance. These results were then used to find the average depth probed below a target radial distance versus detector position.

2.4 True Probe Forward Monte Carlo Model

Because of its ability to recover the reflectance at arbitrary SDDs, the Mono Monte Carlo method was effective for investigating how the number of fibers and their positioning affects optical property recovery in a custom probe. However, certain simplifying assumptions were required during the Monte Carlo simulation. These included

1. A pencil beam photon source instead of a realistic fiber.

2. Cannot use finite size detectors with typical acceptance angles.

3. A semi-infinite medium, which does not account for refractive index variations due to different materials at the surface.

To keep within the small diameter constraint while maximizing the outermost SDD, detector fibers were placed very close to the outer edge of the probe. It was therefore expected that inhomogeneous boundary conditions (the difference in the refractive index of the probe and surrounding air) would have an effect on the reflectance. To investigate this effect, a forward Monte Carlo model was developed, which explicitly simulates the true probe design as closely as possible.

Each fiber was given a circular profile with a refractive index of 1.46, a representative value provided by an optical fiber manufacturer (CeramOptec Industries Inc., East Longmeadow, MA). Each fiber used for diffuse reflectance measurements was given a core diameter of 200 microns. This size was chosen as a tradeoff between maximizing the SDD of the outermost fiber and minimizing the required exposure time. Larger fibers would reduce the maximum achievable SDD and affect the performance of the optical property recovery algorithm, while smaller fibers would require longer measurement times to achieve an acceptable signal-to-noise ratio.

The source fiber was simulated by emitting photons randomly at any point within its core, at any angle within its numerical aperture. Similarly, only photons incident on a detector fiber core at a (refracted) angle within the numerical aperture were scored by the model. Photons incident on the epoxy region of the probe were removed from the simulation (absorbed by the epoxy), while those reaching the tissue surface outside of the probe diameter were reflected according to the Fresnel equations at a boundary with mismatched refractive indices of 1.4 and 1.

The results of this true probe simulation were fitted using the previously described Mono Monte Carlo method to see if it was capable of recovering the input optical properties. This was done over a range of optical properties.

2.5 Hybrid Reflectance Recovery Algorithm

To accurately model the reflectance that will be measured with our probe design, a true probe Monte Carlo simulation is required. Because it is not spatially invariant, however, such a simulation cannot be used to generate the scoring grid in the Mono Monte Carlo model, and therefore a new algorithm for rapid generation of reflectance curves was required. One possible solution would be to generate a two-dimensional look-up table using the forward Monte Carlo model of Sec. 2.4 over a range of μ_s' and μ_a values. Achieving sufficient resolution over the wide range of optical properties listed in Table 1, however, would require a very large number of simulations, and the time required to implement this was considered impractical. Instead, a hybrid look-up table/Mono Monte Carlo method was developed for rapid generation of reflectance curves. This allowed the use of true probe simulations but required fewer simulations than a pure look-up table approach.

The Monte Carlo simulations described in Sec. 2.4 were run for selected values of μ_s', but with μ_a set to 0. Detected photons were scored according to the detector in which they were collected and x_t, the total three-dimensional path length traversed while in the tissue. Combining the results of these simulations produced the three-dimensional grid shown in Fig. 2: the reflectance in each detector for each different value of μ_{sref}' and x_t.

In a process similar to the one in Sec. 2.2, this grid could later be used to recover the reflectance corresponding to a measurement on a sample with arbitrary optical properties. The absorption coefficient of the sample was incorporated by applying Eq. (2), thus collapsing the grid in one dimension. This created a look-up table of the reflectance collected by each detector versus μ_{sref}'. Finally, reflectance values were extracted from this table by interpolating between μ_{sref}' values by cubic splines. This procedure is shown graphically in the Appendix.

$$R(\mu_a) = \sum_{x_t} R_{\text{ref}}(x_t) \cdot e^{-\mu_a \cdot x_t}. \tag{2}$$

In an experimental situation, the optical properties of a tissue sample can be recovered by generating successive spatially resolved reflectance curves with this algorithm and using Marquardt–Levenberg curve-fitting to find the best fit to measured data. By changing the geometry used in the initial Monte
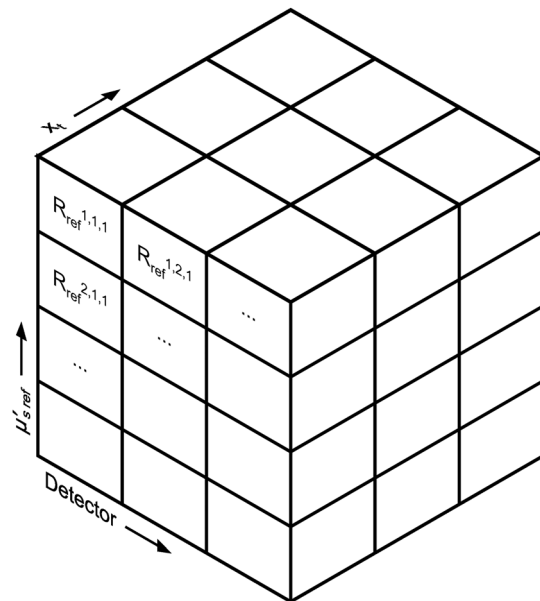

Fig. 2 The photon scoring grid used in the hybrid reflectance recovery algorithm. A number of different simulations were run for different values of μ_s'. Photons in each simulation were scored according to the detector bundle in which they were collected and x_t, the total three-dimensional path length traveled in the tissue.

Carlo simulations, this algorithm could be applied to any desired probe design.

To ensure accuracy in reflectance curves generated with this algorithm, a number of parameters were investigated and optimized. Because photons were scored in discrete bins based on the total path length, both the maximum path length scored and the width of the bins (path length resolution) were parameters of the model. Simulations were run in which photons were scored at very high resolutions of 1×10^4 bins/mm and maximum path lengths of 150 mm. While these values would be impractical for use in a final algorithm due to time and file size constraints, they were used in initial investigations to allow for independent evaluation of each parameter. The optical properties used in these investigations were $\mu_a = \{0.01, 0.5\}$ and $\mu_s' = \{0.5, 13\}$. The four combinations of these values covered the range of optical properties of brain tissue listed in Table 1.

The influence of the maximum path length (x_m) was investigated by finding the total reflectance recovered for a series of x_m values and comparing this to the reflectance when the path length was not limited. The path length resolution was investigated by progressively summing the contents of adjacent bins to simulate coarser binning. Finally, since each simulation used to generate the grid was run with a different value of μ_s'; the resolution in μ_s' was another parameter of the model (the range was previously defined as 0.5 to 13 mm^{-1}). This resolution was progressively improved by running additional simulations and observing plots of the total reflectance versus μ_s'. This procedure was continued until intermediate data points could be accurately interpolated by cubic splines. The error in interpolation was estimated by consecutively removing each point from the data (except the endpoints) and interpolating for the value of the missing data point.

2.6 Optical Property Recovery Performance

Using the Marquardt–Levenberg curve-fitting routine with absolute reflectance data from the hybrid reflectance recovery algorithm will allow recovery of μ_a and μ_s' from measured SR-DRS data. A simulation-based testing procedure was used to characterize the precision of the optical property algorithm. The relative uncertainty (defined here as the standard deviation divided by the mean of 1000 runs) in the recovered optical properties was observed when simulated reflectance curves corrupted by random noise were input to the algorithm.

3 Results and Discussion

3.1 Monte Carlo Model

Results of the comparison between our basic Monte Carlo model, the MCML code,[23] and diffusion theory are shown in Fig. 3 for selected optical properties. It can be observed that at short SDDs (Fig. 3 inset) the results are consistent with MCML, while at longer distances, the results are consistent with both MCML and diffusion theory.

3.2 Reduced Probe Size

The results of the investigation described in Sec. 2.3 (reducing the probe diameter) are shown in Fig. 4, which plots the percent uncertainty in the recovered optical properties versus the maximum SDD in the simulated probe design. These results indicated that the presence of random noise in the reflectance curves had a strong effect on the precision of the optical properties recovered by the Mono Monte Carlo algorithm. The relative
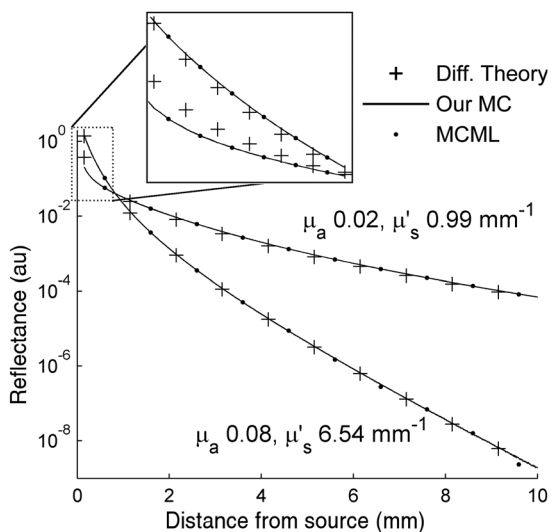

Fig. 3 Validation of Monte Carlo codes. Solid lines are spatially resolved diffuse reflectance spectroscopy (SR-DRS) reflectance curves generated using the Mono Monte Carlo method. Dots indicate the results of the MCML code by Wang et al.[23] Crosses show the results of diffusion theory calculations using the extended source model described by Farrell et al.[37]
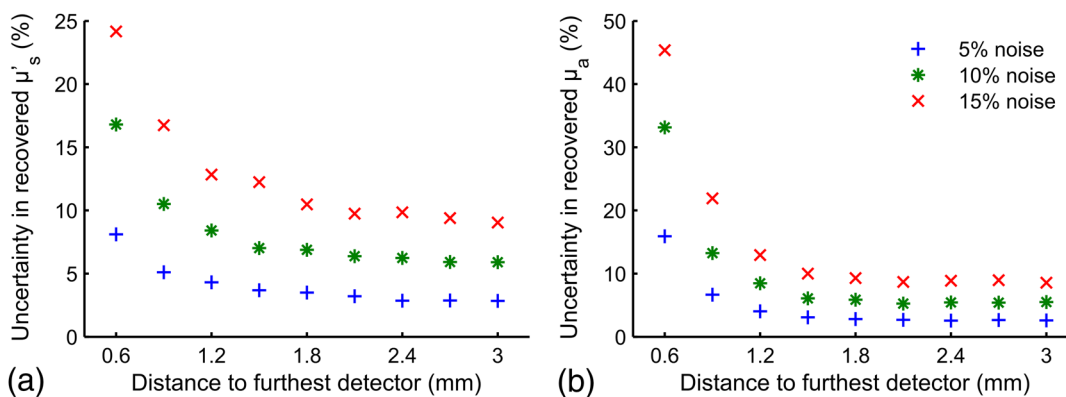

Fig. 4 The percent uncertainty (standard deviation divided by the mean) in the value of the optical properties recovered from 1000 reflectance curves corrupted by normally distributed random noise with a standard deviation of 5, 10, or 15% as indicated. Optical properties of $\mu_a = 0.31$ mm^{-1} and $\mu_a = 2.34$ mm^{-1} were used to generate all initial reflectance curves.
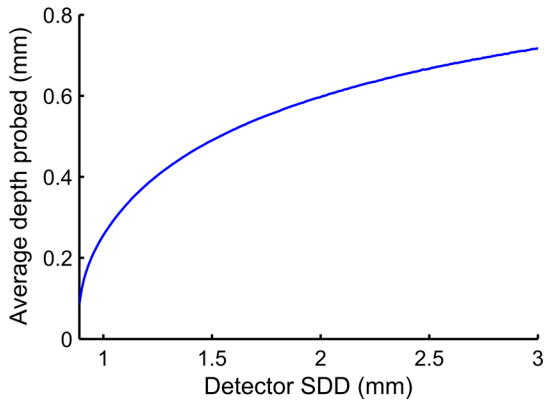
Fig. 5 The influence of the source to detector distance on the depth of tissue probed by DRS. The average depth of tissue probed below a radial distance of 0.89 mm is shown for optical properties of $\mu_a = 0.31$ mm^{-1} and $\mu_a = 2.34$ mm^{-1}.

Table 2 Relative signal strength in each of the outer two diffuse reflectance spectroscopy detector bundles of the probe shown in Fig. 6, obtained through Monte Carlo simulations. This was defined as the total reflectance (photons per unit area) collected in all fibers of the indicated bundle divided by the total reflectance in the detector bundle 0.23 mm from the source.

Tissue	λ (nm)	$[R(0.59 \text{ mm})]/[R(0.23 \text{ mm})]$	$[R(1.67 \text{ mm})]/[R(0.23 \text{ mm})]$
White matter	360	0.337	0.024
	630	0.547	0.213
	950	0.526	0.236
Gray matter	360	0.073	5×10^{-4}
	630	0.179	0.008
	950	0.304	0.023

uncertainty in the recovered optical properties was found to increase approximately linearly with the standard deviation of the added noise and to vary approximately inversely with the SDD of the outermost detector. Examination of Fig. 4 suggests that, for the optical properties shown, an outermost distance ≥1.5 mm would demonstrate acceptable precision. This was consistent with other simulations using different optical properties (data not shown). It can also be observed that at short SDDs, the uncertainty in μ_a is significantly greater than μ_s'. At short SDDs, collected photons have experienced short path lengths in tissue, and therefore the influence of small changes in μ_a is insignificant.

The effect that reducing the maximum SDD had on the depth probed by reflectance measurements is demonstrated by the simulation results in Fig. 5. This shows the average depth probed by photons as they passed below a radial distance of 0.89 mm when the detector was placed at various SDDs.

Using these data alongside other practical constraints, a design with three detectors placed up to a maximum SDD of
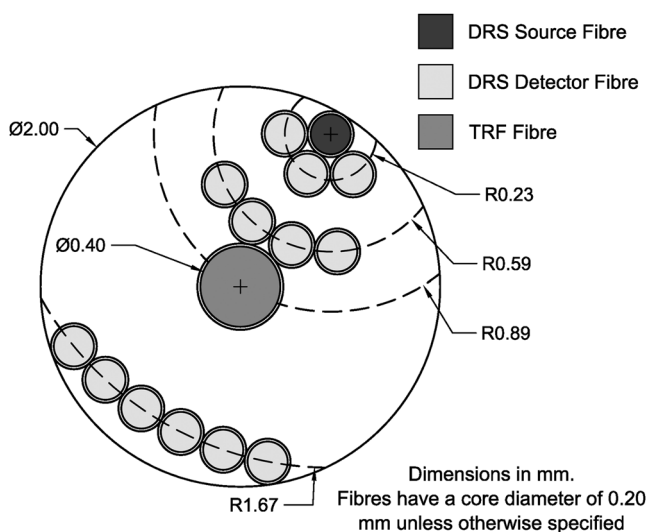
1.67 mm was chosen for use in brain tissue. The furthest detector was placed near to the outer edge of the probe to maximize its SDD, and the diameter of the probe was limited to <2 mm to allow easy manipulation in a small surgical cavity.

Multiple detector fibers were placed at each SDD, and their outputs were bundled together to improve the photon collection efficiency. More fibers were placed in bundles at further SDDs to help compensate for the decreased signal at these distances. The design chosen for the probe is shown in Fig. 6, and the relative signal strength collected by each detector bundle is shown in Table 2.

A 0.4-mm diameter fiber was included in the probe design for future use in a combined diffuse reflectance/time-resolved fluorescence instrument. Although photons entering this fiber were not scored during Monte Carlo simulations, its presence was considered because it altered the reflectance profile of the probe due to a difference in the index of refraction of the fiber and the surrounding probe surface.

3.3 Boundary Effects

The consequences of ignoring the change in refractive index at the probe's edge (boundary effects) are demonstrated in Fig. 7.
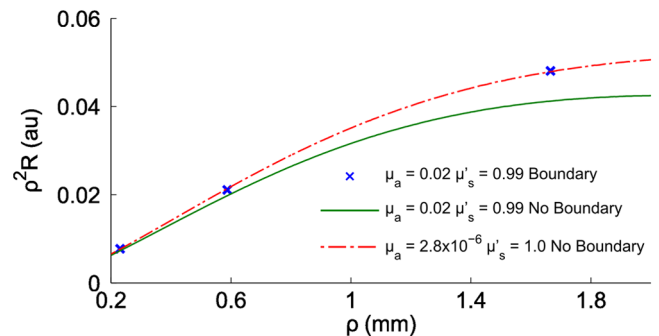

Fig. 6 The proposed design for the fiber optic probe. DRS detector fibers are bundled together into three groups, each at the indicated distance from the DRS source fiber (measured from the centers of each fiber). The central fiber is used for both illumination and detection in time-resolved fluorescence spectroscopy measurements.

Fig. 7 The effects of boundary conditions on optical property recovery with the Mono Monte Carlo algorithm. The solid line is the reflectance curve predicted by the Mono Monte Carlo model for optical properties of $\mu_a = 0.02$ mm^{-1} and $\mu_s' = 0.99$ mm^{-1}. Points marked with an "x" show the reflectance predicted by the true probe forward Monte Carlo model for the same optical properties. The dotted line is the fit generated with the Mono Monte Carlo algorithm, which corresponds to optical properties of $\mu_a = 2.8 \times 10^{-6}$ mm^{-1} and $\mu_s' = 1.0$ mm^{-1}.

Table 3 The effects of boundary conditions on the Mono Monte Carlo algorithm's ability to recover optical properties.

Tissue	λ (nm)	Target optical properties (mm^{-1})		Recovered optical properties (mm^{-1})		Percent difference	
		μ_a	μ_s'	μ_a	μ_s'	μ_a	μ_s'
White matter	360	0.31	2.34	0.29	2.39	−6.45	2.17
	630	0.02	0.99	2.9×10^{-6}	1.00	−99.98	1.54
	950	0.04	0.61	0.02	0.62	−39.40	1.54
Gray matter	360	0.23	12.30	0.23	11.96	−0.92	−2.79
	630	0.08	6.54	0.05	7.12	−31.86	8.90
	950	0.10	3.60	0.08	3.73	−23.75	3.53

Note: The "Target optical properties" were used to generate reflectance curves with a model that simulates the probe boundary. "Recovered optical properties" are the values returned when fitting this simulated data with a model that does not consider boundary conditions. Source–detector distances of 0.23, 0.59, and 1.67 mm were used.

These results show that although the Mono Monte Carlo algorithm was able to generate a good fit to the (simulated) true probe reflectance, this fit corresponds to incorrect optical properties. This analysis was performed over a range of optical properties, and results are listed in Table 3. The discrepancies between the target and recovered absorption coefficients in Table 3 show the strong influence of boundary effects on this probe design. This motivated the development of a new optical property recovery algorithm, one that considers the true geometry of the probe surface. This algorithm was described in Sec. 2.5.

3.4 Parameter Optimization: Hybrid Reflectance Recovery Algorithm

Selected results from the investigation of the maximum path length parameter are shown in Fig. 8. It was found that for path lengths <150 mm, the reflectance in each detector reached >99% of its maximum value, the total when the path length was not limited. This was true for all investigated optical properties (data not shown), and therefore 150 mm was chosen as the maximum path length to record in all simulations.
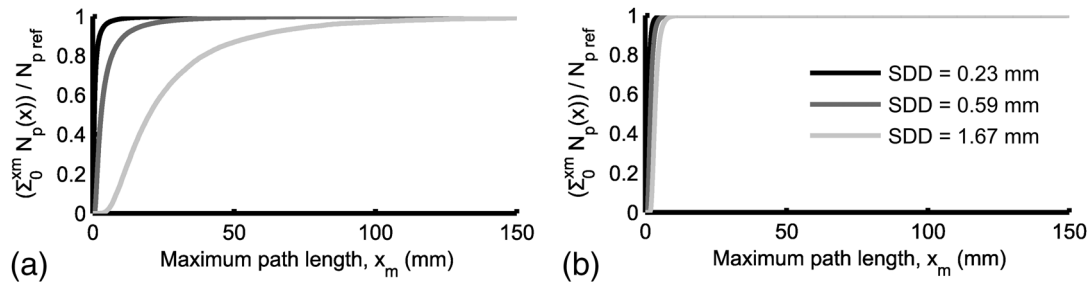

Fig. 8 Investigation of the maximum path length parameter for simulations with optical properties of (a) $\mu_a = 0.01$ mm^{-1}, $\mu_s' = 13$ mm^{-1} and (b) $\mu_a = 0.5$ mm^{-1}, $\mu_s' = 0.5$ mm^{-1}. Each curve corresponds to a simulated detector bundle with the indicated source-to-detector distance. $N_p(x)$ is the number of photons collected that traveled a total path length equal to x. N_{pref} is the total number of photons collected for each source–detector distance (SDD) when the path length was not limited.

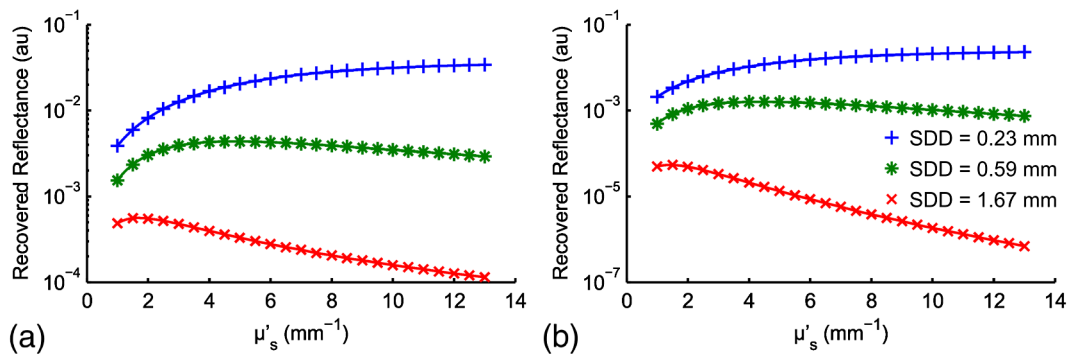**Fig. 9** The reflectance recovered using the method described in Sec. 2.5 for each detector bundle in the probe layout of Fig. 6. Results are shown over a range of desired μ_s' values, with $\mu_a = 0.01$ mm^{-1} (a) and 0.5 mm^{-1}. (b) Data points indicate the μ_{sref}' values used to generate the grid and the lines are the results of interpolation by cubic splines. The error in each data point was <2%.
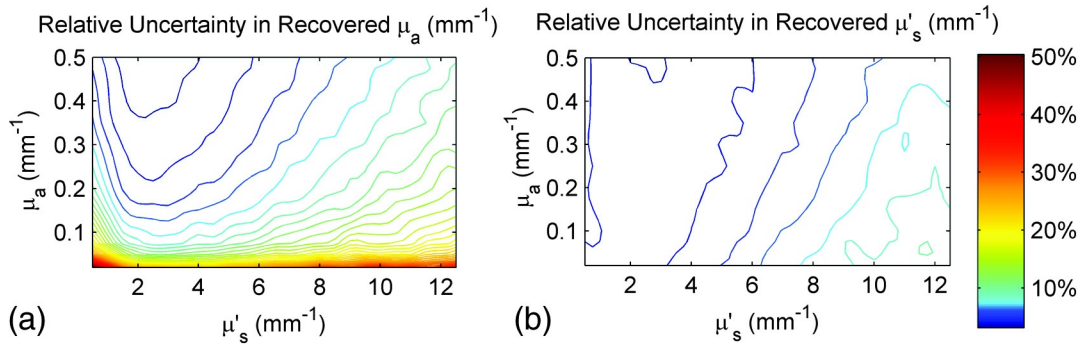
Fig. 10 Performance of the optical property recovery algorithm when presented with simulated reflectance curves corrupted by random noise with a standard deviation of 5%. The values on the x and y axes are the target optical properties, while the contour lines represent the relative uncertainty in the recovered optical properties, defined as the standard deviation of the results divided by the mean over 1000 runs.

Investigation of the path length resolution parameter showed that when it was decreased to 13 bins/mm, the simulated reflectance remained within 1% of the reflectance at 1×10^4 bins/mm. This was true across the range of investigated optical properties, and therefore a path length resolution of 13 bins/mm was selected for x_t. Since the maximum path length recorded was 150 mm, 1950 path length bins were used in total.

The resolution in μ_s' is shown in Fig. 9 for $\mu_a = 0.02$ and 0.5 mm^{-1}. The error in each point was found to be <2% when the resolution in μ_s' was set to 0.5 mm^{-1}.

3.5 Optical Property Recovery Performance

Results characterizing the precision of the optical property recovery algorithm are shown in Fig. 10. All reflectance data used in the fitting procedure corresponded to the probe design of Fig. 6. As expected, the highest uncertainty in the results occurs when recovering the absorption coefficient from data corresponding to low μ_a values. This is a consequence of using a probe with short SDD values; the algorithm is less sensitive to changes in μ_a than μ_s. This is especially true for tissues with very low absorption because of the shape of the corresponding reflectance curve.

4 Conclusion

Monte Carlo simulations were used to determine the minimum diameter of a fiber-optic probe meant for the recovery of optical properties from spatially resolved diffuse reflectance spectra. This was investigated over the wide range of optical properties expected in brain tissue, and the minimum diameter was found to be 1.5 mm. It was discovered that for small probe designs in which detector fibers are placed close to the edge, the true geometry of the probe must be simulated and the different refractive indices at the tissue surface must be considered. A hybrid look-up table/Mono Monte Carlo algorithm was developed to efficiently generate reflectance data that account for the true geometry of the probe. Fitting these data to measured SR-DRS data will allow optical property recovery in brain tissue.

These methods were used to develop a novel, small-diameter fiber-optic probe design for use in a DRS instrument. Simulations with expected signal-to-noise ratios indicated acceptable performance across the range of optical properties of brain tissue. Although the data presented here are for a specific probe design, the algorithm could be readily adapted for any desired probe geometry. The algorithm is compatible with small-diameter probes that are easy to manipulate in surgical cavities.
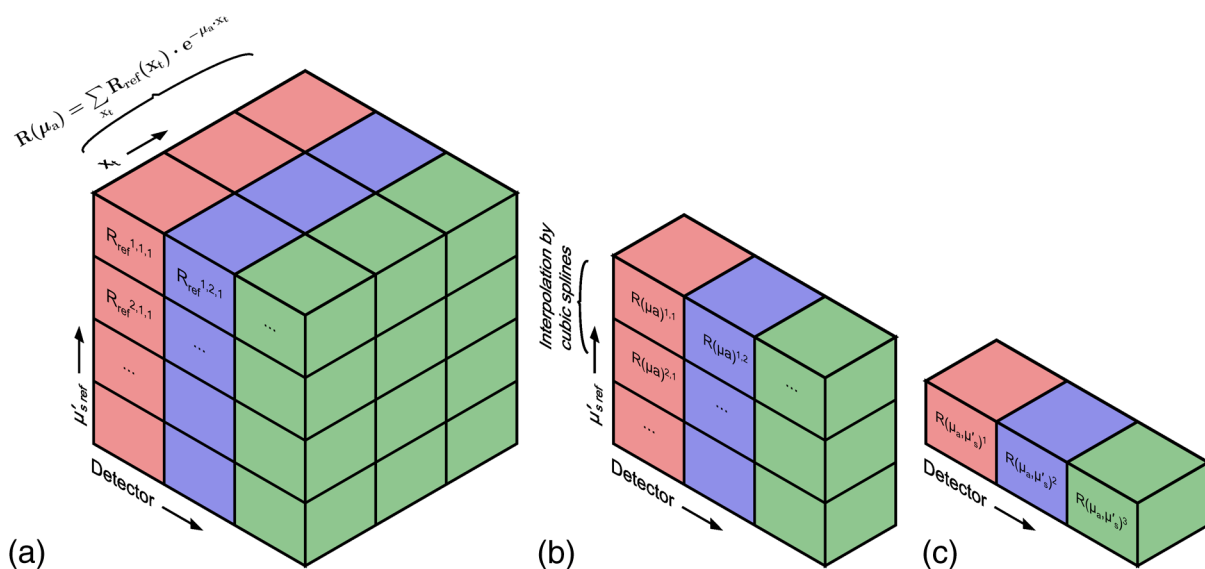
Fig. 11 The true probe inverse reflectance recovery process. (a) The grid is collapsed in one dimension by applying Eq. (2) to incorporate the target μ_a value. (b) The target value of μ_s' is incorporated by interpolating between μ_{sref}' values, thus collapsing the grid further. (c) The expected reflectance collected by each detector when performing a measurement on a sample with optical properties μ_a and μ_s'.

(a)

μ_s'(mm^{-1})	R_{ref} (x_t = 1.462 mm)	R_{ref} (x_t = 1.538 mm)	R_{ref} (x_t = 1.615 mm)	R_{ref} (x_t = 1.692 mm)
0.5	3.848x10^{-5}	3.683x10^{-5}	3.616x10^{-5}	3.506x10^{-5}
1.0	7.947x10^{-5}	7.122x10^{-5}	6.604x10^{-5}	5.952x10^{-5}
1.5	1.072 x10^{-4}	9.884x10^{-5}	8.723x10^{-5}	7.737x10^{-5}
2.0	1.288 x10^{-4}	1.181x10^{-4}	1.043x10^{-4}	9.392x10^{-5}

(b)

$$R(\mu_a) = \sum_{x_t} R_{ref}(x_t) \cdot e^{-\mu_a x_t}$$

$$R(\mu_a = 0.01, \mu_s' = 0.5) = 3.848x10^{-5} \cdot e^{-0.01x1.462} + 3.683x10^{-5} \cdot e^{-0.01x1.538} + \ldots$$

$$R(\mu_a = 0.01, \mu_s' = 1.0) = 7.947x10^{-5} \cdot e^{-0.01x1.462} + 7.122x10^{-5} \cdot e^{-0.01x1.538} + \ldots$$

(c)

μ_s' (mm^{-1})	$R(\mu_a = 0.01$ mm^{-1})
0.5	1.442x10^{-5}
1.0	2.719x10^{-4}
1.5	3.649x10^{-4}
2.0	4.383x10^{-4}

(d)

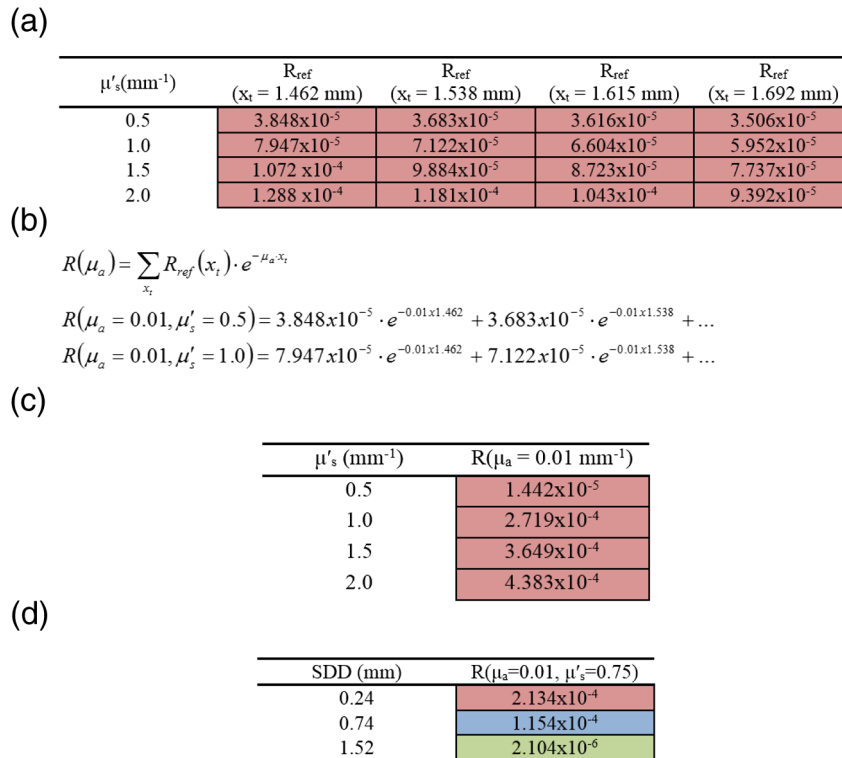| SDD (mm)	$R(\mu_a=0.01, \mu_s'=0.75)$
0.24	2.134x10^{-4}
0.74	1.154x10^{-4}
1.52	2.104x10^{-6}

Fig. 12 A worked example showing the process of reflectance recovery from the true probe simulating grid for optical properties of $\mu_a = 0.01$ and $\mu_s' = 0.75$ mm^{-1}. (a) The reflectance collected by the closest detector (SDD = 0.24 mm) is recovered. Selected data are shown in the table for $\mu_s' = 0.5$ to 2, and path lengths of 1.462 to 1.692 mm. (b) Equation (2) is applied to incorporate the absorption $\mu_a = 0.01$, thus collapsing each row of the table. (c) Data are interpolated by cubic splines to incorporate the scattering, $\mu_s' = 0.75$. (d) This procedure is applied for all three source–detector separations in the probe.

Appendix: Reflectance Recovery Example

A worked example showing the process of recovering the reflectance from the true probe simulating grid is shown in Figs. 11 and 12 for optical properties of $\mu_a = 0.01$ and $\mu_s' = 0.75$ mm^{-1}.

References

1. M. S. Eljamel, G. Leese, and H. Moseley, "Intraoperative optical identification of pituitary adenomas," *J. Neurooncol.* **92**(3), 417–421 (2009).
2. K. M. Davis et al., "Intraoperative ultrasound can decrease the re-excision lumpectomy rate in patients with palpable breast cancers," *Am. Surg.* **77**(6), 720–725 (2011).
3. J. S. Wu et al., "Transsphenoidal pituitary macroadenomas resection guided by PoleStar N20 low-field intraoperative magnetic resonance imaging: comparison with early postoperative high-field magnetic resonance imaging," *Neurosurgery* **65**(1), 63–71 (2009).
4. D. S. Oh and P. M. Black, "A low-field intraoperative MRI system for glioma surgery: is it worthwhile?," *Neurosurg. Clin. N. Am.* **16**(1), 135–141 (2005).
5. W. Stummer et al., "Extent of resection and survival in glioblastoma-multiforme: identification of and adjustment for bias," *Neurosurgery* **62**(3), 564–576 (2008).
6. M. L. C. van Veelen et al., "Supratentorial low grade astrocytoma: prognostic factors, dedifferentiation, and the issue of early versus late surgery," *J. Neurol. Neurosurg. Psychiatry* **64**(5), 581–587 (1998).
7. Z. Volynskaya et al., "Diagnosing breast cancer using diffuse reflectance spectroscopy and intrinsic fluorescence spectroscopy," *J. Biomed. Opt.* **13**(2), 024012 (2008).
8. J. Q. Brown et al., "Quantitative optical spectroscopy: a robust tool for direct measurement of breast cancer vascular oxygenation and total hemoglobin content in vivo," *Cancer Res.* **69**(7), 2919–2926 (2009).
9. R. A. Schwarz et al., "Noninvasive evaluation of oral lesions using depth-sensitive optical spectroscopy," *Cancer* **115**(8), 1669–1679 (2009).
10. D. C. G. de Veld et al., "Autofluorescence and diffuse reflectance spectroscopy for oral oncology," *Lasers Surg. Med.* **36**(5), 356–364 (2005).
11. S. A. Toms et al., "Intraoperative optical spectroscopy identifies infiltrating glioma margins with high sensitivity," *J. Neurosurg.* **57**(4), 382–391 (2005).
12. P. A. Valdes et al., "Quantitative fluorescence in intracranial tumor: implications for ALA-induced PpIX as an intraoperative biomarker," *J. Neurosurg.* **115**(1), 11–17 (2011).
13. W. Stummer et al., "Fluorescence-guided surgery with 5-aminolevulinic acid for resection of malignant glioma: a randomised controlled multicentre phase III trial," *Lancet Oncol.* **7**(5), 392–401 (2006).
14. A. Dhar et al., "Elastic scattering spectroscopy for the diagnosis of colonic lesions: initial results of a novel optical biopsy technique," *Gastrointest. Endosc.* **63**(2), 257–261 (2006).
15. M. D. Keller et al., "Autofluorescence and diffuse reflectance spectroscopy and spectral imaging for breast surgical margin analysis," *Lasers Surg. Med.* **42**(1), 15–23 (2010).
16. I. J. Bigio et al., "Diagnosis of breast cancer using elastic-scattering spectroscopy: preliminary clinical results," *J. Biomed. Opt.* **5**(2), 221–228 (2000).
17. T. Svensson et al., "Characterization of normal breast tissue heterogeneity using time-resolved near-infrared spectroscopy," *Phys. Med. Biol.* **50**(11), 2559–2571 (2005).
18. J. B. Fishkin et al., "Frequency-domain photon migration measurements of normal and malignant tissue optical properties in a human subject," *Appl. Opt.* **36**(1), 10–20 (1997).
19. M. Gurfinkel, T. Pan, and E. M. Sevick-Muraca, "Determination of optical properties in semi-infinite turbid media using imaging measurements of frequency-domain photon migration obtained with an intensified charge-coupled device," *J. Biomed. Opt.* **9**(6), 1336–1346 (2004).
20. A. Kim and B. C. Wilson, "Measurement of ex vivo and in vivo tissue optical properties: methods and theories," in *Optical-Thermal Response of Laser-Irradiated Tissue*, A. J. Welch and M. J. C. van Gemert, Eds., pp. 267–319, Springer, Netherlands (2011).

21. A. Kim et al., "A fiberoptic reflectance probe with multiple source-collector separations to increase the dynamic range of derived tissue optical absorption and scattering coefficients," *Opt. Express* **18**(6), 5580–5594 (2010).

22. S. T. Flock et al., "Monte Carlo modeling of light propagation in highly scattering tissues. I. Model predictions and comparison with diffusion theory," *IEEE Trans. Biomed. Eng.* **36**(12), 1162–1168 (1989).

23. L. Wang, S. L. Jacques, and L. Zheng, "MCML—Monte Carlo modeling of light transport in multi-layered tissues," *Comput. Methods Programs Biomed.* **47**(2), 131–146 (1995).

24. R. Graaff et al., "Condensed Monte Carlo simulations for the description of light transport," *Appl. Opt.* **32**(4), 426–434 (1993).

25. A. Kienle and M. S. Patterson, "Determination of the optical properties of turbid media from a single Monte Carlo simulation," *Phys. Med. Biol.* **41**(10), 2221–2227 (1996).

26. Y. Yuan et al., "High-throughput acousto-optic-tunable-filter-based time-resolved fluorescence spectrometer for optical biopsy," *Opt. Lett.* **34**(7), 1132–1134 (2009).

27. M. G. Müller et al., "Intrinsic fluorescence spectroscopy in turbid media: disentangling effects of scattering and absorption," *Appl. Opt.* **40**(25), 4633–4646 (2001).

28. S. C. Kanick et al., "Extraction of intrinsic fluorescence from single fiber fluorescence measurements on a turbid medium," *Opt. Lett.* **37**(5), 948–950 (2012).

29. C. M. Gardner, S. L. Jacques, and A. J. Welch, "Fluorescence spectroscopy of tissue: recovery of intrinsic fluorescence from measured fluorescence," *Appl. Opt.* **35**(10), 1780–1792 (1996).

30. G. M. Palmer and N. Ramanujam, "Monte-Carlo-based model for the extraction of intrinsic fluorescence from turbid media," *J. Biomed. Opt.* **13**(2), 024017 (2008).

31. J. Wu, M. S. Feld, and R. P. Rava, "Analytical model for extracting intrinsic fluorescence in turbid media," *Appl. Opt.* **32**(19), 3585–3595 (1993).

32. D. J. Cappon et al., "A novel optical property recovery algorithm for use in the optical biopsy of brain tissue," in *Biomedical Optics*, OSA Technical Digest, Optical Society of America, Miami, FL (2012).

33. L. G. Henyey and J. L. Greenstein, "Diffuse radiation in the Galaxy," *Astrophys. J.* **93**, 70–83 (1941).

34. S. Prahl et al., "A Monte Carlo model of light propagation in tissue," *Proc. SPIE* **5**, 102–111 (1989).

35. C. Zhu et al., "Diagnosis of breast cancer using fluorescence and diffuse reflectance spectroscopy: a Monte-Carlo-model-based approach," *J. Biomed. Opt.* **13**(3), 034015 (2008).

36. A. N. Yaroslavsky et al., "Optical properties of selected native and coagulated human brain tissues in vitro in the visible and near infrared spectral range," *Phys. Med. Biol.* **47**(12), 2059–2073 (2002).

37. T. J. Farrell, M. S. Patterson, and B. Wilson, "A diffusion theory model of spatially resolved, steady-state diffuse reflectance for the noninvasive determination of tissue optical properties in vivo," *Med. Phys.* **19**, 879–888 (1992).

38. G. M. Palmer and N. Ramanujam, "Monte Carlo-based inverse model for calculating tissue optical properties. Part I: Theory and validation on synthetic phantoms," *Appl. Opt.* **45**(5), 1062–1071 (2006).